Accelerated Oxygen Exchange Kinetics on $Nd_2NiO_{4+\delta}$ Thin Films with Tensile Strain along *c*-Axis

Nikolai Tsvetkov,[†,‡] Qiyang Lu,[†,§] Yan Chen,[†,‡] and Bilge Yildiz*[,†,‡,§]

[†]Laboratory for Electrochemical Interfaces, [‡]Department of Nuclear Science and Engineering, [§]Department of Materials Science and Engineering, Massachusetts Institute of Technology, 77 Massachusetts Avenue, Cambridge, Massachusetts 02139, United States

ABSTRACT The influence of the lattice strain on the kinetics of the oxygen reduction reaction (ORR) was investigated at the surface of $Nd_2NiO_{4+\delta}$ (NNO). Nanoscale dense NNO thin films with tensile, compressive and no strain along the *c*-axis were fabricated by pulsed laser deposition on single-crystalline $Y_{0.08}Zr_{0.92}O_2$ substrates. The ORR kinetics on the NNO thin film cathodes was investigated by electrochemical impedance spectroscopy at 360–420 °C in air. The oxygen exchange kinetics on the NNO films with tensile strain along the *c*-axis was found to be 2–10 times faster than that on the films with compressive strain along the *c*-axis. A larger concentration of oxygen interstitials (δ) is found in the tensile NNO films compared to the films with no strain or compressive strain, deduced from the measured chemical capacitance. This is consistent with the increase in the distance between the NdO rock-salt layers observed by transmission electron microscopy. The surface structure of the nonstrained and tensile strained films remained stable upon annealing in air at 500 °C, while a significant morphology change accompanied by the enrichment of Nd was found at the surface of the films with compressive strain. The faster ORR kinetics on the tensile strained NNO films was attributed to the ability of these films to incorporate oxygen interstitials more easily, and to the better stability of the surface chemistry in comparison to the nonstrained or compressively strained films.

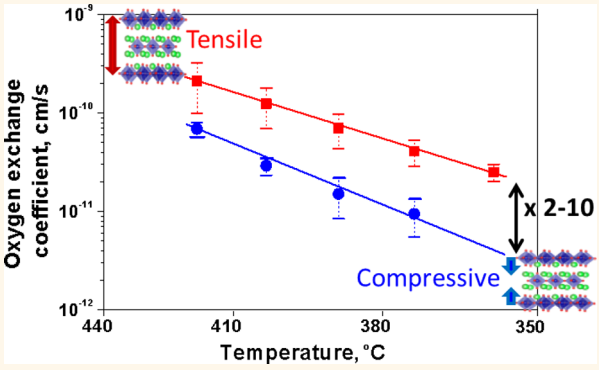

KEYWORDS: lattice strain · nanoscale thin film · electrochemistry · fuel cells · oxygen reduction reaction · Ruddlesden–Popper oxide

The oxygen reduction reaction kinetics is important for determining the performance of catalyst and electrode materials for sustainable energy technologies, including fuel cells,[1,2] photocatalysis,[3] and batteries.[4] Particularly for advancing solid oxide fuel cells (SOFC), discovery of oxide materials with fast kinetics of oxygen reduction reaction (ORR) and fast transport of oxygen ions in the intermediate (500–700 °C) temperature range is needed.[2] Traditionally, attempts to accelerate ORR kinetics in SOFC cathodes has been based on designing and optimizing the bulk material composition and structure.[5,6] More recently, lattice strain has received considerable attention to serve as a new design parameter for accelerating the electrocatalytic reactions by altering the energy landscape of a given material.[7–9] Several examples from the fields of polymer electrochemistry and metal catalysis demonstrate that chemical reactivity can be affected by the change of the length and strength of atomic bonds in the material.[10–13] Perovskite type oxides (ABO_3) are widely studied as SOFC cathodes, but the effect of strain on their reactivity to ORR has not been thoroughly explored. For example, for (La,Sr)MnO_3 (LSM) and $LaCoO_3$(LCO), elastic strain was found to distort the BO_6 octahedra, giving rise to unusual magnetic and electronic properties.[14,15] Regarding the SOFC cathode functionality of the same materials under elastic strain, computational and experimental studies have demonstrated changes in the electronic structure, and in the concentration and mobility of oxygen vacancies as a function of strain.[16,17] For $La_{0.6}Sr_{0.4}CoO_{3-\delta}$ (LSC) in particular, these changes were found to give rise to significant acceleration of the surface oxygen exchange kinetics and of oxygen diffusion

* Address correspondence to byildiz@mit.edu.

Received for review November 3, 2014 and accepted January 23, 2015.

Published online January 24, 2015
10.1021/nn506279h

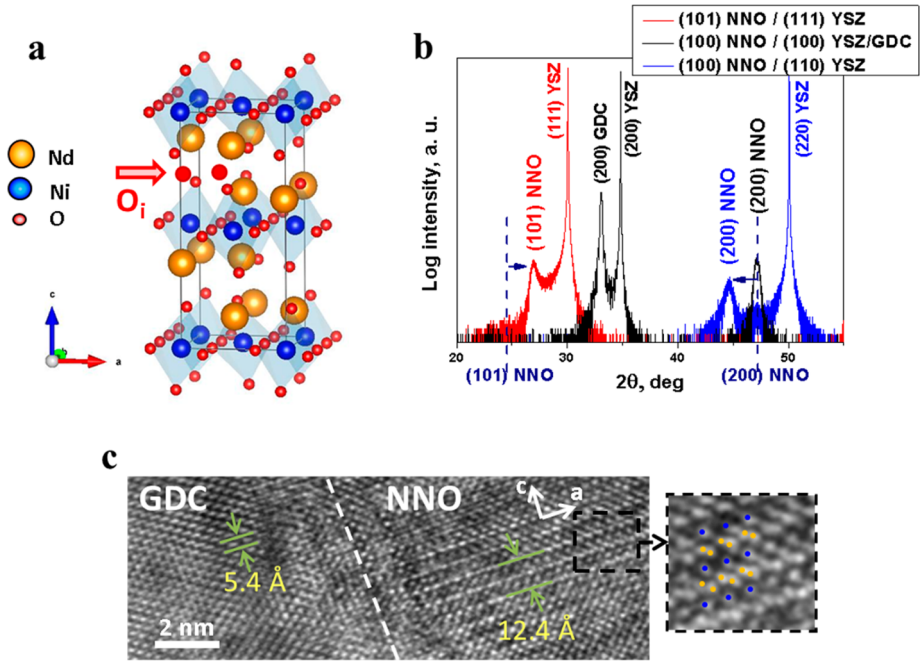

Figure 1. (a) Crystal structure of Nd_2NiO_4 visualized using the VESTA software.[28] The arrow points toward the path of the oxygen interstitials (O_i) that are schematically shown between the NdO layers. (b) XRD pattern on NNO thin films deposited onto YSZ substrates with different orientations. Dashed lines show the reference positions of (200) and (101) peaks for bulk NNO. (c) High resolution TEM (HRTEM) image of the NNO/GDC interface on the (100) YSZ substrate. The positions of the Nd and Ni atoms are shown in the inset with the yellow and blue dots, respectively.

kinetics on epitaxially tensile strained films compared to compressively strained films.[18] These previous results provide a promising scenario for the use of lattice strain in nanoscale structures to accelerate ORR kinetics in oxide electrocatalysis, and they also motivate this paper into looking at anisotropic oxides. LSM and LSC have isotropic and oxygen-vacancy mediated oxygen diffusion and exchange kinetics. On the other hand, anisotropic family of oxides, which have oxygen interstitials for diffusion and surface exchange reactions, has not been investigated under strain systematically prior to our work.

Anisotropic Ruddlesden–Popper (RP) phase materials such as Pr_2NiO_4 and Nd_2NiO_4 have attracted increasing interest as promising cathode materials due to their fast oxygen exchange and diffusion kinetics, which surpass that of the state-of-the-art perovskites.[19−23] Unlike oxygen deficient perovskites, the oxygen reduction in the RP phase materials involves the incorporation and migration of oxygen interstitials. The RP structure consists of perovskite blocks separated by a rock-salt layer. The spacing along the rock-salt layer serves as a fast pathway for oxygen interstitial diffusion[19,24] (Figure 1a). It is known that the incorporation of the oxygen interstitials into these rock-salt layers increases the *c*-lattice parameter,[25] a phenomenon called chemical expansion.[26] Here, *our hypothesis* is that the exchange and diffusion of oxygen can be made easier by enlarging (tensile straining) the distance between the NdO rock-salt layers along the *c*-axis.

In this study we chose the Nd_2NiO_4 (NNO) as a model RP phase material because it is known to have fast oxygen exchange and diffusion kinetics.[20] NNO thin films with tensile and compressive strain along the *c*-axis were fabricated by pulsed laser deposition on the (111)- and (110)-oriented single-crystalline $Y_{0.08}Zr_{0.92}O_2$ (YSZ) substrates, respectively. NNO films with no strain along the *c*-axis were obtained on (100) YSZ substrates with a $Gd_{0.2}Ce_{0.8}O_2$ (GDC) interlayer. The effect of strain on the ORR reactivity was investigated by electrochemical impedance spectroscopy. The stability of the surface chemistry on strained NNO films was investigated by scanning electron microscopy and X-ray photoelectron spectroscopy. The results obtained indicate that the strain introduced by different substrates alters the distance between NdO rock-salt layers and the oxygen overstoichiometry. ORR reactivity at the surface of the NNO films was shown to be enhanced by tensile and hindered by compressive strain along the *c*-axis. The strain-dependence of the ORR reactivity is explained based on the ease of the incorporation of oxygen interstitials into the rock-salt layers and based on the stability of the surface chemistry.

RESULTS AND DISCUSSION

Characterization of Lattice Parameters in Nd_2NiO_4 Thin Films. High-resolution X-ray diffraction (HRXRD) and transmission electron microscopy (TEM) measurements and analysis were performed to determine the crystal structure and to evaluate the strain state along the *c*-axis of the NNO films grown on the YSZ substrates

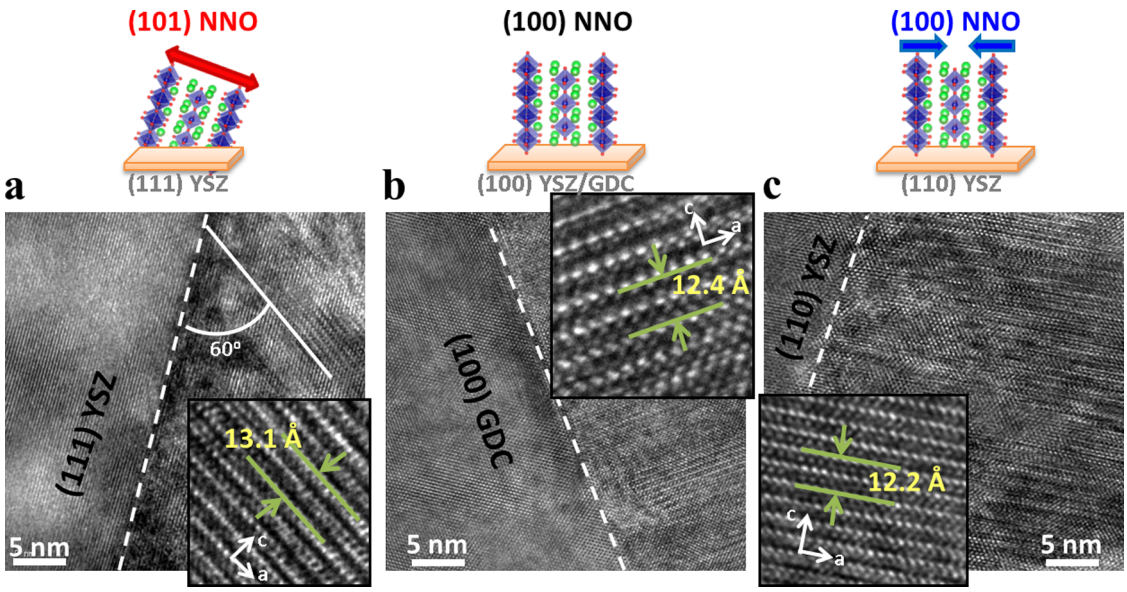

Figure 2. TEM images of the $Nd_2NiO_{4+\delta}$ films deposited on (a) (111) YSZ, (b) (100) YSZ/GDC, and (c) (110) YSZ substrates, with tensile, no (zero), and compressive strain along their *c*-axis, respectively, accompanied by the schematic drawings of NNO films with different orientations and strain types. Representative HRTEM images of the NNO films are shown in insets.

with different orientations. The schematic crystal structure of NNO with the layers of Nd and Ni atoms perpendicular to *c*-axis is shown in Figure 1a. Three different strain states were obtained; nonstrained, tensile and compressive along the *c*-axis when deposited on (100), (111), and (110) YSZ single crystal substrates, respectively. A $Gd_{0.2}Ce_{0.8}O_2$ (GDC) thin film interlayer was necessary on the (100) YSZ substrate to achieve the NNO films with no strain. As will be seen from the TEM images below, the strain induced by different substrates affects the *c*-lattice parameter of the NNO films by alternating the distance between NdO rock salt layers.

Figure 1b shows the HRXRD $2\theta-\omega$ scan patterns used to characterize the orientation and out-of-plane parameters of the fabricated thin films. Along with the intense substrate peaks, the Bragg diffraction peaks of the NNO films were found at 2θ angles of 46°, 44°, and 26° for the films grown on the (100)YSZ/GDC, (110) and (111) YSZ substrates, respectively. It is difficult to make a conclusion about the NNO thin film orientation and strain type only based on the results of the XRD patterns shown in Figure 1b, because some of the diffraction peaks from NNO of different orientations are located within a narrow 2θ range. For example, according to the reference pattern[27] the NNO peak at $2\theta = 46°$ can be attributed to multiple orientations such as (200), (204) or (240). Moreover, a substrate-induced lattice strain of NNO can also lead to the shift of the film peaks from the reference positions, and complicate the analysis.

TEM measurements were performed in order to determine the orientation and to estimate the lattice parameter of NNO films. The (100) NNO/GDC interface on (100) YSZ substrate is shown as an example in Figure 1c. The layered structure of the NNO film, where the columns of bright dots are perpendicular to the NNO/GDC interface can be clearly seen. The bright dots are associated with Nd positions and less bright dots with the Ni. The layers of bright dots observed in the images are the NdO rock-salt layers which are perpendicular to the NNO/GDC interface. Considering the configuration of the NNO film on the (100) GDC interlayer (Figure 1c), it can be concluded that the *c*-axis of the NNO is parallel to the NNO/GDC interface, or equivalently parallel to the (100) YSZ substrate. Thus, the film orientation is (100), denoted as (100) NNO/(100) YSZ/GDC in Figure 1b.

Lattice parameter along the *c*-axis of all the NNO films was estimated from the TEM images (Figures 1c and 2a–c). The in-plane lattice parameter of the NNO on (100) YSZ/GDC was calculated as 12.4 Å (Figure 2b). There exists a range of lattice parameters (12.1–12.6 Å) reported for bulk, unstrained $Nd_2NiO_{4+\delta}$ specimens in literature,[27,29–32] depending on the value of δ that was quenched to room temperature. The XRD pattern measured for our NNO polycrystalline target (powder sample) is matched closest by refs 27 and 30, which give a *c*-axis lattice parameter of 12.4 Å for the bulk, unstrained NNO. Therefore, we take the 12.4 Å as the reference, nonstrained *c*-axis lattice parameter. At the same time the obtained GDC substrate lattice parameter of 5.4 Å is in good agreement with the reference lattice parameter of GDC. Both the TEM and XRD measurements showed no deviation of the lattice parameter from the reference state for the (100) NNO film on the (100) YSZ/GDC substrate. Thus, we can designate this NNO film to have no lattice strain along its *c*-axis.

The orientation and the *c*-lattice parameter of the NNO films deposited on (110) YSZ and (111) YSZ

substrates were determined in a similar way as described above for NNO film on the (100) YSZ/GDC substrate. For the NNO films on (110) YSZ, the NdO rock-salt layers are perpendicular to the NNO/YSZ interface, corresponding to the NNO film orientation of (100) (Figure 2c). The *c*-lattice parameter was found to be of around 12.2 Å (Figure 2c), indicating that the film is compressively strained along the *c*-axis. It is known that compressive strain along the *c*-axis of NNO results in the increase of the *a*-lattice parameter[25] which is the out-of-plane lattice parameter for (100) NNO. The out-of-plane lattice parameter was determined from the HRXRD pattern. Indeed, the shift of the (200) reflection peak to the lower 2θ region is observed in Figure 1b. This shift indicates that the out-of-plane lattice parameter is tensile strained. Thus, from the results of both the TEM and XRD analysis, the NNO film on the (110) YSZ was found to be compressively strained along the *c*-axis.

For NNO film deposited on (111) YSZ, the NdO rock-salt layers are tilted by around 60° with respect to the NNO/YSZ interface, corresponding to the NNO film orientation of (101). From TEM measurements of the NNO/(111) YSZ sample, the lattice parameter along the *c*-axis was found to be 13.1 Å, larger than that in the reference nonstrained state. Thus, we can conclude that the *c*-axis of this film is tensile-strained. This result is also in good agreement with the shift of the diffraction peak to higher 2θ values (Figure 1b), showing that the out-of-plane direction (that involves the (ab) plane of the (101) NNO) is compressively strained.

In summary, consistency of the results obtained from XRD and TEM allows us to conclude that the NNO thin films have three different strain states along their *c*-axis. Specifically, these are the nonstrained (100) NNO film on the (100) YSZ/GDC substrate, (100) NNO film with a compressive strain of around 2% along its *c*-axis on the (111) YSZ substrate, and (101) NNO film with a tensile strain of around 6% along its *c*-axis on the (111) YSZ substrate.

It is worth noting that the interface between YSZ and NNO is not coherent and has defects, as shown in the TEM images. This is not unexpected due to the large mismatch between the lattice parameters of YSZ and NNO.[33] However, despite the partial relaxation of the lattice strain from the interfaces, we observe a large difference in the strain state of these films, ranging from −2 to 6% along the *c*-axis. We believe this could be due, in part, to the ability of the different films to equilibrate with different amount of oxygen interstitials. Thus, the different substrates here do not strictly determine the lattice parameters of the NNO films by an epitaxial relation. The large range of strain in these NNO films is then due to a combination of a direct effect from the substrate (although partially relaxed) and the effect of oxygen stoichiometry (as will be quantified later in this paper).

Oxygen interstitials cannot be directly visualized in conventional TEM images. However, the observable deformation of the lattice because of the large size of the oxygen interstitials can be used as a signature of the presence of these point defects in TEM images. Zhang *et al.*, by combining TEM and neutron diffraction measurements, have shown that the presence of oxygen interstitials in silica apatite leads to the appearance of dark spots in HRTEM micrographs and to the formation of the local distortions in the lattice.[34] Here, we cannot use the appearance of dark spots as a measure of oxygen interstitial content, because the FIB milling used for the fabrication of the TEM samples can also form similar defects. However, we have found that the separation distance between the NdO rock-salt layers vary systematically with strain, and this variation is correlated to the amount of oxygen interstitials present in the films, consistent with the previous studies of chemical expansion in the bulk of this material.[25] The increase of the *c*-lattice parameter in tensile strained NNO on the (111) YSZ substrate is found primarily due to the increase of the distance between NdO layers (marked as ΔNdO in Figure 3). The size of perovskite blocks (denoted as NiO_6 in Figure 3) remains nearly the same for all three strain types, while ΔNdO increases from compressive to tensile NNO films. This result is in good agreement with the known

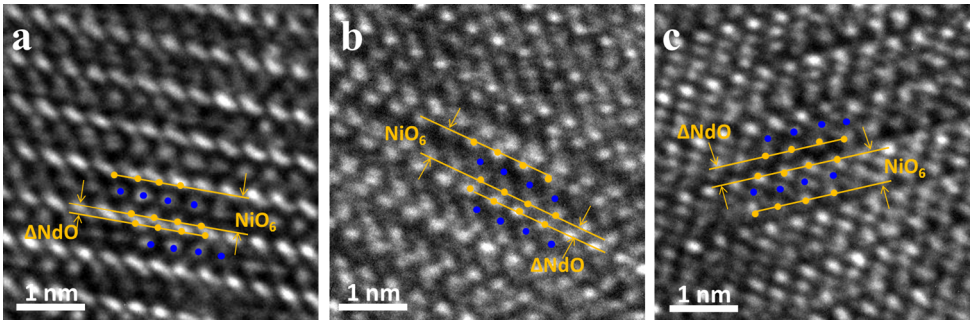

Figure 3. HRTEM images of the $Nd_2NiO_{4+\delta}$ films: (a) compressively strained (100) NNO on (110) YSZ, (b) nonstrained (100) NNO on (100) YSZ/GDC, and (c) tensile strained (101) NNO on (111) YSZ substrates. The positions of Nd and Ni atoms are denoted with the yellow and blue dots, respectively. ΔNdO indicates the distance between the NdO rock salt layers, NiO_6 represent the size of the perovskite block. ΔNdO increases from compressive to tensile NNO films, while the NiO_6 remains unchanged.

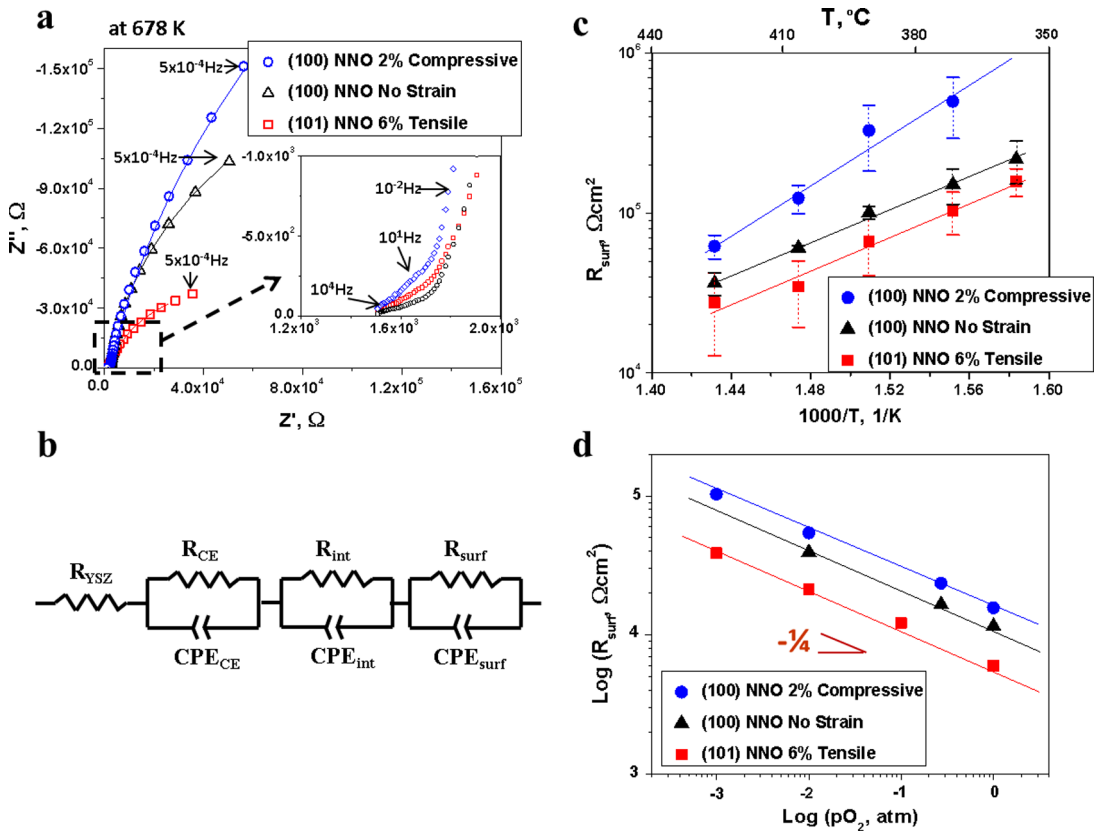

Figure 4. (a) Typical impedance spectrum of the cells with the $Nd_2NiO_{4+\delta}$ thin film cathodes at 678 K in air. Solid lines are the fitting curves. High frequency region of Nyquist plot is shown in the inset. (b) Equivalent circuit[33] used for analysis of the EIS data. Area specific resistance of oxygen surface exchange reaction at the surface (R_{surf}) as a function of (c) inverse temperature in air (shown data at each temperature span the range of R_{surf} values obtained for two different sets of samples), and (d) oxygen partial pressure at 773 K.

location of oxygen interstitials, that is along the rock-salt layers of RP phase materials,[25,35] and implies that the increase in lattice parameter along the *c*-axis is accompanied by incorporation of more oxygen interstitials in our NNO films (this point will be later shown in Figure 6).

Oxygen Exchange Kinetics As a Function of Strain. The effect of lattice strain on the ORR kinetics was evaluated by comparing the area specific resistance (ASR) of the oxygen exchange reaction measured by electrochemical impedance spectroscopy (EIS) on NNO thin film cathodes. The NNO thin film cathodes tested here are the compressively strained (100) NNO on (110) YSZ, the nonstrained (100) NNO on (100)YSZ/GDC, and the tensile strained (101) NNO on (111) YSZ substrates, as described above. The (101) NNO films with tensile strain along their *c*-axis demonstrated faster oxygen exchange kinetics in comparison to that on (100) NNO nonstrained or compressively strained films.

The typical impedance response of the cells with NNO thin film cathodes is shown in Figure 4a. EIS response of NNO/YSZ/Ag cells can be modeled with circuit made of three R//C elements, or more generally three R//CPE (resistor in parallel to constant phase element) (Figure 4b).[33,36] The largest arc in the lower frequency region, R_{surf}, is known to reflect the oxygen exchange reaction at the cathode surface.[33,36,37] As presented below, the most significant differences among the differently strained NNO cathode films arises in their R_{surf}. The feature in the middle frequency range can be attributed to oxygen diffusion in the cathode layer[33] or across the electrolyte/cathode interface.[38] We performed measurements of the NNO/YSZ/Ag cells with two different NNO thicknesses (20 and 200 nm) and did not find any significant difference in the middle frequency feature as a function of thickness (Figure S1, Supporting Information). Thus, this element, R_{int}, was attributed to the resistance at the substrate/NNO interface. The suppressed semicircle in the high frequency range is at least 2 orders of magnitude smaller that the main semicircle in the low frequency range, R_{surf}, and its activation energy is around 0.9 eV. The high frequency feature of the EIS response, R_{CE}, can be attributed to the Ag counter electrode or electrical contacts. The extracted R_{YSZ} (Figure 4c) values, which represents the position of the highest frequency intercept at the z'-axis, are in the good agreement with the literature data on YSZ conductivity (Figure S2).[39]

In this work, R_{surf} was found to be the lowest for the NNO films with tensile strain and the highest for the NNO films with compressive strain along their *c*-axis (Figure 4c). Within 360−420 °C in air, the R_{surf} values for the tensile NNO films were found to be 2−10 times

smaller compressive NNO films. Tensile strain increases the separation distance along the rock-salt layers, *i.e.*, the ΔNdO in Figure 3, and opens a larger volume for easier incorporation of oxygen interstitials from the surface. The average activation energy for the oxygen exchange reaction was estimated to be around 1.0 ± 0.1 eV for the tensile strained (101) NNO and for the nonstrained (100) NNO, and around 1.3 ± 0.1 eV for the compressively strained (100) NNO. The higher activation energy of R_{surf} on the compressively strained NNO films is likely due to the higher energy barrier to incorporating oxygen interstitials into the narrower rock-salt layers.

The R_{int} values for the nonstrained (100) NNO on (100) YSZ/GDC and tensile strained (101) NNO on (111) YSZ are similar (Figure S2).The R_{int} was found significantly larger for the (100) NNO on (101) YSZ substrate. This can be due to presence of the barrier for oxygen migration from the compressively strained NNO to YSZ, as hypothesized in ref 33. The R_{CE} values for all the three NNO film cathodes were similar to each other (Figure S2).

The oxygen partial pressure (pO_2) dependence of the R_{surf} of the NNO films is presented in the Figure 4d. For all the films, the plots of R_{surf} *versus* pO_2 demonstrate a slope of −1/4. This means that the electron transfer from NNO to the adsorbed oxygen, for example, $O + 2e^- \leftrightarrow O^{2-}$, is the rate limiting step for ORR. This is a typical behavior of p-type mixed electronic ionic conductors such as Pr_2CuO_4[40] or $Sr(Ti,Fe)O_3$.[41]

The electrical surface oxygen exchange coefficient, k^q, can be determined from the R_{surf} values according to the equation[38]

$$k^q = \frac{(k_B T)}{(4e^2 c_0 R_{surf})}$$

where k_B is the Boltzmann constant, T is the temperature, e is the electronic charge, and c_0 is the total concentration of lattice oxygen determined according to data from the study of Nakamura *et al.*[25] The calculated values for k^q for the different sets of samples are shown in Figure 5. The surface exchange coefficient on the tensile (101) NNO films is 2−10 times higher than the compressive (100) NNO films. We are also comparing this data with the k^q values that are calculated from the EIS data reported by Yamada *et al.* for compressively strained (110) NNO films (which also have the *c*-axis in plane) on YSZ substrates.[33] The surface exchange kinetics reported in this work and by Yamada *et al.* for compressive NNO films are consistent with each other.

We attribute the faster exchange kinetics of oxygen on the tensile (101) NNO films in part to their ability to incorporate and equilibrate a larger amount of interstitials. This is because the tensile strain along the *c*-axis is accommodated by the enlargement of the distance between the NdO rock-salt layers, as shown by TEM in Figure 3, indicating larger oxygen excess for this material.[25] To support this, we estimated

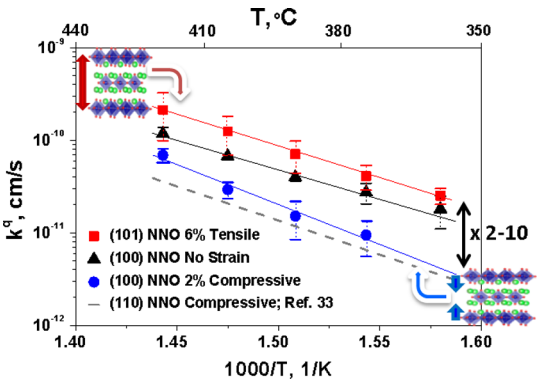

Figure 5. Surface exchange coefficient, k^q, of the $Nd_2NiO_{4+\delta}$ films with different strain types as a function of inverse temperature in air (shown data at each temperature span the range of k^q values obtained for two different sets of samples). Dashed line indicates the k^q values calculated from the R_{surf} data from the work of Yamada *et al.*[33]

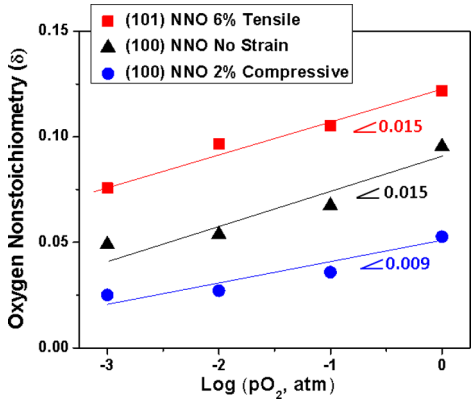

Figure 6. Oxygen nonstoichiometry, δ, calculated from the chemical capacitance of the $Nd_2NiO_{4+\delta}$ films with different strain types as a function of oxygen pressure, pO_2, at 773 K.

the oxygen nonstoichiometry, δ, in NNO films by measuring the chemical capacitance[42−45] values from EIS. The details of the analytical approach and the calculations are given in the Section 2 of Supporting Information. Figure 6 shows the dependence of δ on oxygen partial pressure, pO_2, for the NNO films with different strain states at 773 K. It can be clearly seen that the films with tensile strain can indeed accommodate a substantially larger oxygen excess than the nonstrained or compressively strained films; ∼3 times more at 10^{-3} atm and more than ∼2.5 times more at 1 atm.

Surface Stability As a Function of Strain. To investigate the effect of strain on the stability of the surface chemistry of NNO films, the cation composition and morphology of the NNO film surfaces were investigated before and after annealing at 773 K for 10 h in air. We have shown that the nonstrained and tensile strained NNO film surfaces remain stable during heat treatment, while a Nd-rich phase segregation at the surface was found for the film with compressive strain along the *c*-axis.

TABLE 1. Nd/Ni Ratio Calculated from the Analysis of The Nd 3d and Ni 2p X-ray Photoelectron Spectra on $Nd_2NiO_{4+\delta}$ Films with Different Types of Strain[a]

	all films, as-fabricated	annealed (100) NNO no strain	annealed (101) NNO 6% tensile	annealed (100) NNO 2% compressive
Nd/Ni	2.0	2.2	2.3	2.8

[a] "Annealed" states refer to the surfaces after being subjected to 773 K for 10 h in air.

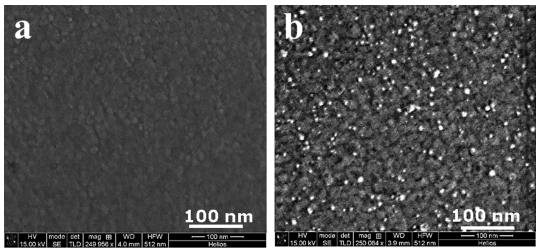

Figure 7. Scanning electron microscopy images of surface morphology on $Nd_2NiO_{4+\delta}$ films. (a) Typical morphology for all the as-prepared specimens before annealing, and for the (100) NNO with no strain and (101) NNO with 6% tensile strain after heat treatment at 773 K in air for 10 h; and (b) morphology on (100) NNO with 2% compressive strain after heat treatment at 773 K in air for 10 h.

Nd/Ni ratio deduced from X-ray photoelectron spectroscopy measurements on the NNO films is summarized in Table 1 for different strain states. Regardless of the strain type all the as-fabricated films shows Nd/Ni ratio very close to its stoichiometric value of 2. After annealing, a significant increase in the Nd content was observed for the films with the compressive strain, while Nd/Ni ratio remains close to the stoichiometric value on the nonstrained and tensile-strained NNO films. Thus, we can conclude that the Nd segregation at the film surface depends on the strain type.

The segregation of cations, as reflected from the increase of Nd/Ni ratio, can be accompanied by phase separation and morphological changes at the surface, as shown for other perovskites in our previous work.[46,47] Figure 7 shows the surface morphology on NNO films with the different types of strain after annealing at 773 K in air for 10 h, imaged by scanning electron microscopy. All the as-fabricated NNO films were smooth, and exhibited no difference as a function of strain (Figure S4, Supporting Information). After annealing, the nonstrained and tensile strained film surfaces remained smooth without any evidence to formation of observable defects within the resolution limit of these SEM images. The structural stability at the surface is consistent with the relatively stable Nd/Ni ratio shown in Table 1. On the other hand, the compressively strained films exhibited formation of small particles with a diameter of around 5 nm at the film surface (Figure 7b). Concurrent with the increase of Nd/Ni ratio to nearly 3 (Table 1), such appearance of particles indicate formation of Nd-rich phases at the surface. We hypothesize that the elastic energy minimization is a driver for Nd segregation to the surface.[47] Since compressive strain shrinks the NdO rock-salt layers (Figure 3), it can push the relatively large Nd cations to the surface in order to reduce the elastic energy of the system.

CONCLUSION

The experimental results obtained on strained $Nd_2NiO_{4+\delta}$ films demonstrate that lattice strain along the *c*-axis of RP-type oxides can impact the oxygen exchange kinetics at the surface significantly. The tensile strain along the *c*-axis of $Nd_2NiO_{4+\delta}$ enlarges the distance between the NdO rock-salt layers, allowing for a larger volume to incorporate oxygen interstitials more easily compared to nonstrained or compressively strained films. Consistent with this finding, chemical capacitance measurements revealed that the oxygen excess (δ) in tensile $Nd_2NiO_{4+\delta}$ films is more than twice that of compressive $Nd_2NiO_{4+\delta}$ films. Surface chemistry of tensile NNO films is also more stable by avoiding (or minimizing) Nd-rich phase separation at the surface. As a result, the oxygen exchange kinetics is 2−10 times faster on the NNO films with tensile strain in comparison to those with compressive strain, as quantified by electrochemical impedance spectroscopy. Considering that about 50% of the SOFC energy losses come from the ORR reactions at the cathode at 500−600 °C,[48] a gain of 2−10 times in ORR kinetics means a significant gain in SOFC efficiency at those temperatures. Given that the actual strain state in these films is not epitaxial, it should be possible to synthesize strained Ruddlesden−Popper thin film cathodes synthesized by chemical routes onto backbone support architectures in real SOFC devices.[49] Moreover, while these results are demonstrated on $Nd_2NiO_{4+\delta}$, we believe that modulating the rock-salt layer separation by *c*-axis strain in other RP-type oxides would also allow to tune the oxygen exchange reactions at their surfaces and interfaces.

METHODS

Dense $Nd_2NiO_{4+\delta}$ films were deposited onto substrates using PLD method with a KrF excimer laser of 248 nm wavelength. The $Nd_2NiO_{4+\delta}$ target that was used for pulsed laser deposition (PLD) was prepared by the conventional Pechini method starting from neodymium and nickel nitrates powders. The films were deposited at 650 °C under oxygen pressure of 10 mTorr. After the growth process, the films were cooled down to room

temperature in 10 Torr oxygen pressure to oxidize the films. The film thickness was around 25 nm.

Single crystalline (100), (110) and (111) (YSZ) substrates were used for deposition of the NNO films. In case of the (100) YSZ substrate, the 40 nm interlayer of $Gd_{0.2}Ce_{0.8}O_2$ was deposited prior to NNO film growth at the same conditions as the NNO films. Crystal structure and strain state of thin films were identified using Rigaku Smartlab diffractometer equipped with 2-bounce Ge (220) channel-cut monochromator using Cu $K\alpha_1$ radiation. Samples for transmission electron microscopy (TEM) measurements were fabricated in the Helios Nanolab 600 dual beam focused ion beam milling system. TEM samples were fabricated using Ga ion beam operated at a voltage and current that was varied in range of 30 keV-2 keV and 9.5 nA-28 pA, respectively. For the (110) and (111) YSZ substrates the FIB cut was made parallel to the edges with [110] and [111] type directions, respectively. For the (100) YSZ substrate the cutting plane was at 45° with respect to the substrate edge. The same Helios scanning electron microscope (SEM) was used for imaging the surface morphology. TEM measurements were performed using the JEOL 2010 FEG microscope.

Electrochemical impedance spectroscopy (EIS) measurements were performed on asymmetrical cells with the NNO thin film cathodes grown on different YSZ single crystal substrates. Dense platinum current collectors in the form of a grid (which covers 75% of electrode surface with 25 μm × 25 μm openings) were deposited on the NNO thin films by means of photolithography and RF sputtering. Porous Ag layer served as the counter electrode. Parstat 2273 potentiostat was used to perform the EIS measurements in the frequency range of 100 kHz to 0.5 mHz with AC amplitude of 5 mV and zero DC bias at temperatures between 360 and 420 °C in air and at 500 °C at the oxygen partial pressures in the range of 1 to 10^{-3} atm. ZView software was used for the data fitting and analysis.

X-ray photoelectron spectroscopy (XPS) measurements have been performed in order to estimate the surface cation composition, in terms of the Nd/Ni cation ratio, using PerkinElmer PHI-5500 ESCA Spectrometer with monochromated Al Kα (1486.65 eV) X-ray radiation under a base pressure of 10^{-9} Torr. The quantitative analysis of the Nd 3d and Ni 2p XPS spectra was performed using Multipack 9.0 software.

Conflict of Interest: The authors declare no competing financial interest.

Acknowledgment. The authors are grateful for the funding support from NSF CAREER Award of the National Science Foundation, Division of Materials Research, Ceramics Program, Grant No. 1055583. The authors also acknowledge the use of the Center for Materials Science and Engineering, an MRSEC facility of NSF at MIT. This work made use of the MRSEC Shared Experimental Facilities at MIT, supported by the National Science Foundation under award number DMR-08-19762. We thank Dr. Di Chen and Prof. Harry Tuller for constructive discussions on the estimation of oxygen non-stoichiometry from chemical capacitance measurements.

Supporting Information Available: Electrochemical impedance response of the Nd_2NiO_4/YSZ/Ag cells. Calculation of the oxygen nonstoichiometry in $Nd_2NiO_{4+\delta}$ films. Comparison of the electrochemical response of the 20 and 200 nm thick NNO films. Surface stability as a function of strain imaged by SEM. This material is available free of charge *via* the Internet at http://pubs.acs.org.

REFERENCES AND NOTES

1. Jacobson, M. Z.; Colella, W. G.; Golden, D. M. Cleaning the Air and Improving Health with Hydrogen Fuel-Cell Vehicles. *Science* **2005**, *308*, 1901–1905.
2. Steele, B. C. H.; Heinzel, A. Materials for Fuel-Cell Technologies. *Nature* **2001**, *414*, 345–352.
3. Chueh, W. C.; Falter, C.; Abbott, M.; Scipio, D.; Furler, P.; Haile, S. M.; Steinfeld, A. High-Flux Solar-Driven Thermochemical Dissociation of CO_2 and H_2O Using Nonstoichiometric Ceria. *Science* **2010**, *330*, 1797–1801.
4. Tarascon, J. M.; Armand, M. Issues and Challenges Facing Rechargeable Lithium Batteries. *Nature* **2001**, *414*, 359–367.
5. Shao, Z.; Haile, S. M. A High-Performance Cathode for the Next Generation of Solid-Oxide Fuel Cells. *Nature* **2004**, *431*, 170–173.
6. Yokokawa, H.; Horita, T. Chapter 5: Cathodes. In *High Temperature and Solid Oxide Fuel Cells*; Subhash, C. S., Kevin, K., Eds.; Elsevier Science: Amsterdam, 2003; pp 119−147.
7. Yildiz, B. "Stretching" the Energy Landscape of Oxides—Effects on Electrocatalysis and Diffusion. *MRS Bull.* **2014**, *39*, 147–156.
8. Bissett, M. A.; Konabe, S.; Okada, S.; Tsuji, M.; Ago, H. Enhanced Chemical Reactivity of Graphene Induced by Mechanical Strain. *ACS Nano* **2013**, *7*, 10335–10343.
9. Schweiger, S.; Kubicek, M.; Messerschmitt, F.; Murer, C.; Rupp, J. L. M. A Microdot Multilayer Oxide Device: Let Us Tune the Strain-Ionic Transport Interaction. *ACS Nano* **2014**, *8*, 5032–5048.
10. Akbulatov, S.; Tian, Y.; Boulatov, R. Force−Reactivity Property of a Single Monomer Is Sufficient To Predict the Micromechanical Behavior of Its Polymer. *J. Am. Chem. Soc.* **2012**, *134*, 7620–7623.
11. Mavrikakis, M.; Hammer, B.; Nørskov, J. K. Effect of Strain on the Reactivity of Metal Surfaces. *Phys. Rev. Lett.* **1998**, *81*, 2819–2822.
12. Yang, J.; Yang, J.; Ying, J. Y. Morphology and Lateral Strain Control of Pt Nanoparticles *via* Core−Shell Construction Using Alloy AgPd Core Toward Oxygen Reduction Reaction. *ACS Nano* **2012**, *6*, 9373–9382.
13. Sneed, B. T.; Young, A. P.; Jalalpoor, D.; Golden, M. C.; Mao, S.; Jiang, Y.; Wang, Y.; Tsung, C.-K. Shaped Pd−Ni−Pt Core-Sandwich-Shell Nanoparticles: Influence of Ni Sandwich Layers on Catalytic Electrooxidations. *ACS Nano* **2014**, *8*, 7239–7250.
14. Ding, Y.; Haskel, D.; Tseng, Y.-C.; Kaneshita, E.; van Veenendaal, M.; Mitchell, J. F.; Sinogeikin, S. V.; Prakapenka, V.; Mao, H.-k. Pressure-Induced Magnetic Transition in Manganite $La_{0.75}Ca_{0.25}MnO_3$. *Phys. Rev. Lett.* **2009**, *102*, 237201.
15. Rata, A. D.; Herklotz, A.; Nenkov, K.; Schultz, L.; Dörr, K. Strain-Induced Insulator State and Giant Gauge Factor of $La_{0.7}Sr_{0.3}CoO_3$ Films. *Phys. Rev. Lett.* **2008**, *100*, 076401.
16. Han, J. W.; Yildiz, B. Enhanced One Dimensional Mobility of Oxygen on Strained LaCoO (001) Surface. *J. Mater. Chem.* **2011**, *21*, 18983–18990.
17. Cai, Z.; Kuru, Y.; Han, J. W.; Chen, Y.; Yildiz, B. Surface Electronic Structure Transitions at High Temperature on Perovskite Oxides: The Case of Strained $La_{0.8}Sr_{0.2}CoO_3$ Thin Films. *J. Am. Chem. Soc.* **2011**, *133*, 17696–17704.
18. Kubicek, M.; Cai, Z.; Ma, W.; Yildiz, B.; Hutter, H.; Fleig, J. Tensile Lattice Strain Accelerates Oxygen Surface Exchange and Diffusion in $La_{1-x}Sr_xCoO_{3-\delta}$ Thin Films. *ACS Nano* **2013**, *7*, 3276–3286.
19. Bassat, J.-M.; Burriel, M.; Wahyudi, O.; Castaing, R.; Ceretti, M.; Veber, P.; Weill, I.; Villesuzanne, A.; Grenier, J.-C.; Paulus, W.; Kilner, J. A. Anisotropic Oxygen Diffusion Properties in $Pr_2NiO_{4+\delta}$ and $Nd_2NiO_{4+\delta}$ Single Crystals. *J. Phys. Chem. C* **2013**, *117*, 26466–26472.
20. Boehm, E.; Bassat, J. M.; Dordor, P.; Mauvy, F.; Grenier, J. C.; Stevens, P. Oxygen Diffusion and Transport Properties in Non-Stoichiometric $Ln_2NiO_{4+\delta}$ oxides. *Solid State Ionics* **2005**, *176*, 2717–2725.
21. Kilner, J. A. Fast Oxygen Transport in Acceptor Doped Oxides. *Solid State Ionics* **2000**, *129*, 13–23.
22. Kim, G.; Wang, S.; Jacobson, A. J.; Reimus, L.; Brodersen, P.; Mims, C. A. Rapid Oxygen Ion Diffusion and Surface Exchange Kinetics in $PrBaCo_2O_{5+x}$ with a Perovskite Related Structure and Ordered A Cations. *J. Mater. Chem.* **2007**, *17*, 2500–2505.
23. Tarancon, A.; Skinner, S. J.; Chater, R. J.; Hernandez-Ramirez, F.; Kilner, J. A. Layered Perovskites as Promising Cathodes for Intermediate Temperature Solid Oxide Fuel Cells. *J. Mater. Chem.* **2007**, *17*, 3175–3181.

24. Parfitt, D.; Chroneos, A.; Kilner, J. A.; Grimes, R. W. Molecular Dynamics Study of Oxygen Diffusion in $Pr_2NiO_{4+\delta}$. *Phys. Chem. Chem. Phys.* **2010**, *12*, 6834–6836.
25. Nakamura, T.; Yashiro, K.; Sato, K.; Mizusaki, J. Thermally-Induced and Chemically-Induced Structural Changes in Layered Perovskite-Type Oxides $Nd_{2-x}Sr_xNiO_{4+\delta}$ (x = 0, 0.2, 0.4). *Solid State Ionics* **2010**, *181*, 402–411.
26. Marrocchelli, D.; Bishop, S. R.; Tuller, H. L.; Yildiz, B. Understanding Chemical Expansion in Non-Stoichiometric Oxides: Ceria and Zirconia Case Studies. *Adv. Funct. Mater.* **2012**, *22*, 1958–1965.
27. Watanabe, K.; Asakawa, H.; Fujinawa, G.; Ishikawa, K.; Nakamura, T. *X-sen Bunseki no Shinpo* **1998**, *29*, 137–152. Data from ICSD.
28. Momma, K.; Izumi, F. VESTA 3 for Three-Dimensional Visualization of Crystal, Volumetric and Morphology Data. *J. Appl. Crystallogr.* **2011**, *44*, 1272–1276.
29. Arbuckle, B. W.; Ramanujachary, K. V.; Zhang, Z.; Greenblatt, M. Investigations on the Structural, Electrical, and Magnetic Properties of $Nd_{2-x}Sr_xNiO_{4+\delta}$. *J. Solid State Chem.* **1990**, *88*, 278–290.
30. Attfield, M. P.; Battle, P. D.; Bollen, S. K.; Gibb, T. C.; Whitehead, R. J. The Crystal Structure and Magnetic Properties of $SrLaFeSnO_6$ and $SrLaNiSbO_6$. *J. Solid State Chem.* **1992**, *100*, 37–48.
31. Rodriguez-Carvajal, J.; Fernandez-Diaz, M. T.; Martinez, J. L.; Fernandez, F.; Saez-Puche, R. Structural Phase Transitions and Three-Dimensional Magnetic Ordering in the Nd_2NiO_4 Oxide. *EPL Europhys. Lett.* **1990**, *11*, 261.
32. Tamura, S. The Polymorphic Transition of Nd_2NiO_4 from the Monoclinic Form to the Tetragonal. *J. Phys. Soc. Jpn.* **1972**, *33*, 574–574.
33. Yamada, A.; Suzuki, Y.; Saka, K.; Uehara, M.; Mori, D.; Kanno, R.; Kiguchi, T.; Mauvy, F.; Grenier, J.-C. Ruddlesden-Popper-Type Epitaxial Film as Oxygen Electrode for Solid-Oxide Fuel Cells. *Adv. Mater.* **2008**, *20*, 4124–4128.
34. Zhang, Y.; Su, Z.; Azad, A. K.; Zhou, W.; Irvine, J. T. S. Directly Imaging Interstitial Oxygen in Silicate Apatite. *Adv. Energy Mater.* **2012**, *2*, 316–321.
35. Kushima, A.; Parfitt, D.; Chroneos, A.; Yildiz, B.; Kilner, J. A.; Grimes, R. W. Interstitialcy Diffusion of Oxygen in Tetragonal $La_2CoO_{4+\delta}$. *Phys. Chem. Chem. Phys.* **2011**, *13*, 2242–2249.
36. Adler, S. B. Factors Governing Oxygen Reduction in Solid Oxide Fuel Cell Cathodes. *Chem. Rev.* **2004**, *104*, 4791–4844.
37. Jamnik, J.; Maier, J. Generalised Equivalent Circuits for Mass and Charge Transport: Chemical Capacitance and Its Implications. *Phys. Chem. Chem. Phys.* **2001**, *3*, 1668–1678.
38. Baumann, F. S.; Fleig, J.; Habermeier, H.-U.; Maier, J. Impedance Spectroscopic Study on Well-Defined $(La,Sr)(Co,Fe)O_{3-\delta}$ Model Electrodes. *Solid State Ionics* **2006**, *177*, 1071–1081.
39. Goodenough, J. B. Oxide-Ion Electrolytes. *Annu. Rev. Mater. Res.* **2003**, *33*, 91–128.
40. Lyskov, N. V.; Kaluzhskikh, M. S.; Leonova, L. S.; Mazo, G. N.; Istomin, S. Y.; Antipov, E. V. Electrochemical Characterization of Pr_2CuO_4 Cathode for IT-SOFC. *Int. J. Hydrogen Energy* **2012**, *37*, 18357–18364.
41. Jung, W.; Tuller, H. L. A New Model Describing Solid Oxide Fuel Cell Cathode Kinetics: Model Thin Film $SrTi_{1-x}Fe_xO_{3-\delta}$ Mixed Conducting Oxides—a Case Study. *Adv. Energy Mater.* **2011**, *1*, 1184–1191.
42. Kim, G. T.; Wang, S.; Jacobson, A. J.; Chen, C. Impedance Studies of Dense Polycrystalline Thin Films of $La_2NiO_{4+\delta}$. *J. Mater. Chem.* **2007**, *17* (13), 1316–1320.
43. Chen, D.; Bishop, S. R.; Tuller, H. L. Nonstoichiometry in Oxide Thin Films: A Chemical Capacitance Study of the Praseodymium-Cerium Oxide System. *Adv. Funct. Mater.* **2013**, *23* (17), 2168–2174.
44. Kawada, T.; Suzuki, J.; Sase, M.; Kaimai, A.; Yashiro, K.; Nigara, Y.; Mizusaki, J.; Kawamura, K.; Yugami, H. Determination of Oxygen Vacancy Concentration in a Thin Film of $La_{0.6}Sr_{0.4}CoO_{3-\delta}$ by an Electrochemical Method. *J. Electrochem. Soc.* **2002**, *149* (7), E252–E259.
45. Nakamura, T.; Yashiro, K.; Sato, K.; Mizusaki, J. Thermally-Induced and Chemically-Induced Structural Changes in Layered Perovskite-Type Oxides $Nd_{2-x}Sr_xNiO_{4+\delta}$ (x = 0; 0, 0.2, 0.4). *Solid State Ionics* **2010**, *181* (8—10), 402–411.
46. Cai, Z.; Kubicek, M.; Fleig, J.; Yildiz, B. Chemical Heterogeneities on $La_{0.6}Sr_{0.4}CoO_{3-\delta}$ Thin Films—Correlations to Cathode Surface Activity and Stability. *Chem. Mater.* **2012**, *24*, 1116–1127.
47. Lee, W.; Han, J. W.; Chen, Y.; Cai, Z.; Yildiz, B. Cation Size Mismatch and Charge Interactions Drive Dopant Segregation at the Surfaces of Manganite Perovskites. *J. Am. Chem. Soc.* **2013**, *135*, 7909–7925.
48. Zhou, W.; Shao, Z.; Kwak, C.; Park, H. J. Advanced Cathodes for Solid Oxide Fuel Cells. In *Materials for High-Temperature Fuel Cells*; Wiley-VCH Verlag GmbH & Co. KGaA: Berlin, 2013; pp 49—95.
49. Shah, M.; Barnett, S. A. Solid Oxide Fuel Cell Cathodes by Infiltration of $La_{0.6}Sr_{0.4}Co_{0.2}Fe_{0.8}O_{3-\delta}$ into Gd-Doped Ceria. *Solid State Ionics* **2008**, *179*, 2059–2064.